PAPER

Check for updates

Surface thermodynamics of yttrium titanate pyrochlore nanomaterials†

Margaret E. Reece,[a,b] Jiahong Li,[a] Andrew C. Strzelecki,[b,c] Juan Wen, [ID][d]
Qiang Zhang [ID][a] and Xiaofeng Guo [ID] *[a,c]

Nanocrystalline pyrochlore materials have been investigated for their enhanced radiation tolerance as ceramic nuclear waste hosts. In this work, we study the thermodynamic driving force of nano-scale materials for radiation resistance. The size dependent thermodynamic properties of a series of $Y_2Ti_2O_7$ nanoparticles were investigated. Samples were synthesized by a sol–gel method and characterized by synchrotron X-ray diffraction, BET analysis, and thermogravimetric analysis. The surface and interface enthalpies of $Y_2Ti_2O_7$ were determined by high temperature oxide melt drop solution calorimetry to be 4.07 J m^{-2} and 3.04 J m^{-2}, respectively. The experimentally obtained surface energy is in good agreement with computationally derived average surface energies for yttrium and other rare-earth titanate pyrochlores. Theoretical links between nanoparticle stability, surface energy, and radiation resistance of pyrochlore materials were then explored.

1. Introduction

Rare earth element oxide ceramics, particularly pyrochlores, have been investigated for a wide range of applications in thermal barrier coatings,[1–7] catalytic activity,[7–11] solid oxide fuel cells,[12–15] and most extensively as host matrices for actinides in nuclear waste.[16–19] The pyrochlore family boasts a high number of compositions that have been successfully synthesized and studied for chemical durability, waste loading, radiation tolerance, and other related properties.[20–27] Having compositions of $A_2B_2O_7$, the ordered pyrochlore (space group, s.g. $Fd\bar{3}m$) is a derivative of the fluorite structure (s.g. $Fm\bar{3}m$) with two unique cation sites and one-eighth fewer oxygen anions. The most common pyrochlores are made up of larger trivalent cations that occupy the eight-coordinated A-site and smaller tetravalent cations in the six-coordinated B-site.[28–30] $A_2B_2O_7$ can also crystalize as polymorphs other than the ordered pyrochlore, and the phase is dominantly controlled by the size of the cations incorporated in the structure and their coordination environments.[31–40] This flexibility allows for fine-tuning and optimization for incorporating radioactive cations with non-ideal charges or radii through coupling mechanisms as observed in systems with uranium.[29,41]

Most naturally occurring pyrochlores are metamict (partially amorphous) due to the effects of the radioactive decay of ^{238}U, ^{235}U, and ^{232}Th and their daughter products, which can change the incorporation behaviour of actinides.[29,39,42] Radiation, such as β-decay of fission products and α-decay of the actinide elements, can induce point defects (*e.g.*, interstitials and vacancies) that are aggregated for long-range disorder,[32,43–45] which can further cause significant degradation to the material properties (*i.e.*, hardening, embrittlement, swelling) and limit the lifetime of the nuclear waste host.[45,46] Thus, predicting radiation response is critical in evaluating candidate waste forms. Previously, radiation resistance was found to be controlled by composition,[47–50] vacancy inclusion,[51,52] intrinsic disorder,[53–55] and grain size.[56] In this study, we focus on the size effect on the thermodynamic properties of nanoparticles by experimental calorimetry, with extended correlation with radiation resistance.

Radiation-induced point defects aggregate to form long-range disorders in crystalline materials by forming interstitial atom-vacancy pairs. The mobile interstitial atoms have been found to accumulate at crystallite surfaces in bulk materials, with recent molecular dynamics studies showing a short-range recombination of the displaced atoms with vacancies in a mechanism driven by the surface.[52,57–59] While atoms in a bulk crystalline material would be dominantly in the interior that can be better described by the crystal structure, atoms in a nanocrystal may have a substantial portion in the surface

[a]Department of Chemistry, Washington State University, Pullman, WA 99164, USA. E-mail: x.guo@wsu.edu, q.zhang@wsu.edu

[b]Earth and Environmental Sciences Division, Los Alamos National Laboratory, Los Alamos, New Mexico 87545, USA

[c]The School of Mechanical and Materials Engineering, Washington State University, Pullman, WA 99164, USA

[d]School of Materials and Energy, Lanzhou University, Lanzhou, Gansu 730000, China

†Electronic supplementary information (ESI) available. See DOI: https://doi.org/10.1039/d3nr05605h

region, in which the coordination is less than ideal and the atomic bonding environment is unsatisfied.[60,61] At particle sizes decreasing to the nano-scale regime, atoms on the surfaces increasingly dominate over those that reside in the bulk-core. The consequence is that properties of nanosized particles are often different from their bulk counterparts.[62–65] From a thermodynamic point of view, the surface region has different thermodynamic parameters, which differ from that of the bulk phase by the excess free surface energy ($\Delta G_{surface}$) which often contributes endothermically to the thermodynamic stability. As the size of a grain increases from the scale of a single unit cell to a larger grain diameter, the free energy accumulated from the unsatisfied bonds decreases with respect to the bulk material free energy. This results in high contribution from $\Delta G_{surface}$ at low grain sizes and a flattening of this effect at high grain sizes. Thus, nanoparticles due to their metastable nature, tend to reduce $\Delta G_{surface}$ by interacting with external substances, such as formation of agglomerates, binding to ligands and solvent, and chemical reaction with available species.[66] On the other hand, the free energy of irradiated material also depends upon the energy contribution of point defects (ΔG_{defect}) that have accumulated. The defect energy is directly related to the concentration of these point defects, for which there is a kinetically controlled equilibrium of defect formation and annihilation.[57,67] Recombination of interstitial atoms and vacancies is assisted by surfaces, so at small grain diameters, the rate of recombination is greater than that of vacancy formation, while at large diameters it is the opposite.[68–70] The dependence of $\Delta G_{surface}$ and ΔG_{defect} on the particle diameter has been discussed in-depth,[71,72] and is summarized in Fig. 1.

As a result of such an interplay between surface energy and energy related to radiation-induced point defects, the radiation resistance of a nanoparticle can be effectively controlled by tuning size.[71] According to Fig. 1, thermodynamics of small particles with diameters in regions 1 and 2 is dominated by

$\Delta G_{surface}$, with the overall Gibbs free energy higher than the energy barrier for amorphization ($\Delta G_{amorphization}$). For bulk sized particles that reside beyond region 3, the surface energy contribution is not significant and there are insufficient surfaces acting as point defect sinks to prevent cascades, and so the amorphization process is driven by ΔG_{defect}. Thus, with the energetic competition between $\Delta G_{surface}$ and ΔG_{defect}, it is then possible to engineer nanosized ceramics with desired stability within the region 3, such that the total energies, $\Delta G_{surface} + \Delta G_{defect}$, is smaller than $\Delta G_{amorphization}$. In this diameter range, the amorphization of the nanomaterial is thermodynamically unfavourable and hindered.

For solids, the contribution from entropy and excess volume terms are negligible, and so $\Delta G_{surface}$ can be determined by the production of the specific surface free energy (γ) and the surface area (SA).[73]

$$\Delta G_{surface} = \gamma \times SA.$$

Thus, obtaining the specific surface free energy is critical for understanding how a waste form, such as pyrochlore, in the repository responds to irradiation. In this study, we experimentally determined the surface free energy of nanosized $Y_2Ti_2O_7$ pyrochlores by performing high temperature oxide melt drop solution calorimetry. Yttrium was chosen because it is the fourth most abundant rare earth element (REE) and the most abundant heavy rare earth element (HREE),[74] with an ionic radius near the middle of the HREE range.[75] In order to ensure the ordered pyrochlore crystal structure of the material, titanium was selected as the B-site cation. Although zirconium, hafnium, and tin are also common B-site cations, the A/B cationic ratio of yttrium to any of them is below or only just within the stable range to form ordered pyrochlore.[28,29,35,37,75] Additionally, the thermodynamic properties of bulk-sized $Y_2Ti_2O_7$ have been determined thoroughly,[47] yet there are very limited thermodynamic studies of these nanocrystalline pyrochlores.[45,65,76–78] This work represents one of the efforts to experimentally determine surface effects on the thermodynamic stability of pyrochlore, which can shed light on designing novel nanoceramic materials aimed at forming durable nuclear waste hosts.

2. Experimental

2.1 Sample synthesis

Yttrium titanate pyrochlore can be prepared by traditional solid-state reaction methods,[79] coprecipitation,[80] hydrothermal approaches,[81,82] and sol–gel methods.[83] Among these, sol–gel methods adapting the Pechini approach based on polymeric precursors has resulted in a large body of published work with pyrochlore nanomaterials of small size and high phase purity.[45,84–89] Nanocrystalline $Y_2Ti_2O_7$ pyrochlore powders were synthesized according to previously published methods using a modified citric acid sol–gel route described by Chen and Wen (Fig. S1†).[45,85] Starting materials of yttrium oxide (Y_2O_3, 99.99%) was dissolved in nitric acid with slow heating to
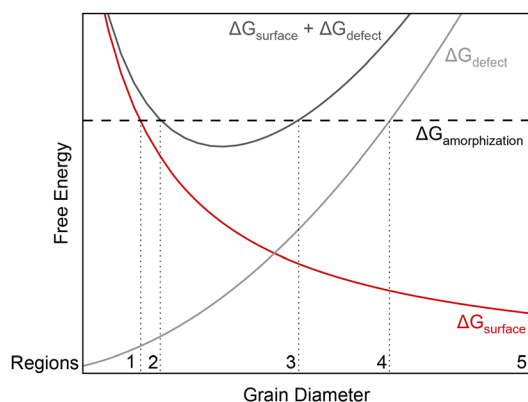

Fig. 1 Descriptions for the free energy of surfaces ($\Delta G_{surface}$), point defects (ΔG_{defect}), and phase amorphization ($\Delta G_{amorphization}$) as a function of grain diameter. Regions for distinguished grain size effects on the free energy of the system are indicated by vertical lines. Recreated from ref. 71.

remove the excess nitrate. A 1:1 stoichiometric molar ratio (Y/Ti) of tetrabutyl titanate was dispersed in a citric acid (CA)–absolute ethanol mixture. The amount of citric acid chelator was calculated such that $nCA/(nY + nTi) = 2.5$. This solution was stirred until homogenous and then combined with the aqueous yttrium nitrate solution under heat and stirring conditions. The mixture became highly viscous and finally changed into a glossy gel that was then allowed to air dry. Heat treatment of the samples was performed in air with the same dwelling time of 1 h at different temperatures from 700–850 °C (one batch every 50 degrees) for obtaining particles with different sizes.

2.2 Characterization

Synchrotron powder X-ray diffraction was conducted at beamline 11-ID-C of the Advanced Photon Source (APS) at Argonne National Laboratory (ANL). The wavelength of the X-ray beam was 0.1173 Å, with a distance of 1610 mm from the sample to the detector. Collected two-dimensional (2D) images were calibrated, integrated, and refined by the Rietveld method using the General Structure Analysis System software version II (GSAS-II),[90] where instrument parameters were obtained using a CeO_2 standard. Backgrounds of these spectra were modelled by the Chebyshev function with 6 coefficients. Procedures for the above Rietveld refinement are referenced elsewhere.[91–95] Brunauer–Emmett–Teller (BET) surface area of the nanosized samples were obtained from the measured nitrogen adsorption–desorption isotherms collected on a Micromeritics ASAP 2020Plus instrument at 77 K. Samples were degassed under vacuum at 150 °C for 10 h before analysis. Transmission electron microscopy (TEM) pictures were acquired using a FEI Tecnai F30 instrument after preparing the samples by dispersing the sample into absolute ethanol with ultrasonic treatment, then dropping the solution onto the carbon-coated TEM grids and naturally drying in air.

2.3 Thermogravimetric analysis

Thermogravimetric analysis coupled with differential scanning calorimetry (TGA-DSC) was performed on a Setaram SetSYS 2400 thermogravimetric differential scanning calorimeter, where 5–20 mg of the sample was heated from 28 to 1000 °C in an alumina crucible with a heating rate of 10 °C min^{-1} under a flowing N_2 atmosphere (20 mL min^{-1}). The temperature and sensitivity of the instrument were calibrated by heating indium, tin, lead, zinc, aluminium, silver, and gold across their fusion point repeatedly at temperature change rates of 5, 10, 15, and 20 °C min^{-1}.[92,96–100]

2.4 High temperature oxide melt solution calorimetry

The enthalpy of drop solution (ΔH_{ds}) was measured directly by a Setaram AlexSYS-1000 Calvet-type microcalorimeter. The calibration of the instrument was conducted by performing transpose temperature drops using solid pieces of α-Al_2O_3. The powdered nanoparticle samples were hand pressed into pellets with masses between 2 and 6 mg, and dropped from room temperature into a molten solvent of sodium molybdate

($Na_2O \cdot MoO_3$) contained in a Pt crucible at 700 °C with bubbling O_2 through the solvent at a rate of 5 mL min^{-1}. The calorimeter chambers were continuously flushed with O_2 gas at a rate of ~100 mL min^{-1} to facilitate a constant gas environment above the solvent. Methods for determination of enthalpies of formation by high temperature oxide melt solution calorimetry employed in this work from enthalpy of drop solution have been previously described in more detail.[101–107]

3. Results and discussion

3.1 Characterization of nanosized particles

X-ray diffraction patterns of the four as-prepared samples clearly show diffraction related to pyrochlore with peaks (Fig. 2 and S2–S4†) such as the (111), (311), (331), and (511). Rietveld refinements were performed using the $Fd\bar{3}m$ space group. The resulting refinements yielded R_{wp} values between 4.1 to 8.5% with average crystallite sizes in the 30–135 nm range. The calculated size was visually confirmed for the 34 and 131 nm size samples by TEM (Fig. S5†). A representative fit of the 131 nm sample is shown in Fig. 2, with all refined results summarized in Table 1. The atomic displacement parameter (U_{iso}) increases as crystallite size decreases for all atoms in the structure. Surface atoms of the material have higher thermal displacement parameters due to their locally unsatisfied bonding environments. The increase in the ratio of surface atoms to bulk atoms as crystallite diameter decreases leads to a greater number of atoms with this lattice distortion in the material, and can be seen in the trend of the atomic displacement parameters. Surface area data determined by BET are also included in Table 1.

TGA of the $Y_2Ti_2O_7$ samples under nitrogen (Fig. S6†) show an extended region of mass loss from 100–500 °C. This extended region of mass loss is expected to attribute to the removal of physically adsorbed species (e.g., water) on the high surface area. Coupled DSC (Fig. S7†) revealed coarsening of
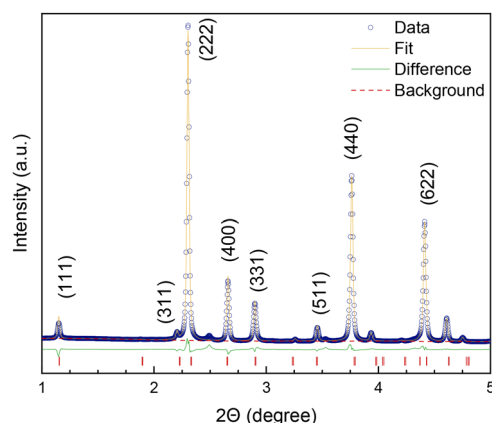

Fig. 2 Representative fit of synchrotron XRD patterns of $Y_2Ti_2O_7$ in the size of 130 nm. Allowed diffraction maxima for pyrochlore phase is represented by *red tick marks*, with specific plane reflections indexed.

Table 1 Summary of XRD and BET parameters

XRD diameter (nm)	Unit cell parameter (Å)	U_{iso} (Å^2/100)				BET surface area (m^2 g^{-1})
		Y 16d	Ti 16c	O′ & O 8b & 8a	O 48f	
30.83(2)	10.1157(6)	2.4(3)	0.58(3)	5.9(2)	4.1(1)	29.0144 ± 0.3443
34.74(8)	10.1376(4)	2.6(2)	0.54(1)	6.1(1)	5.8(2)	23.1521 ± 0.2243
41.56(1)	10.1196(7)	2.1(2)	0.52(4)	4.8(3)	3.9(2)	20.7425 ± 0.1470
131.4(3)	10.1015(2)	1.2(3)	0.46(2)	2.4(1)	2.3(4)	10.6342 ± 0.0173

Errors of values refined from Rietveld analysis are for the last reported digit.

Table 2 Thermochemical cycle for determination of enthalpy of formation from the binary oxides and standard enthalpy of formation for $Y_2Ti_2O_7$ nanoparticles based on drop solution calorimetry

	Reaction	ΔH (kJ mol^{-1})
(1)	$Y_2Ti_2O_7 \cdot xH_2O_{(s,25\,°C)} \rightarrow Y_2O_{3(sln,\,700\,°C)} + 2TiO_{2(sln,\,700\,°C)} + xH_2O_{(g,\,700\,°C)}$	$\Delta H_1 = \Delta H_{ds}{}^a$
(2)	$TiO_{2(s,\,rutile,25\,°C)} \rightarrow TiO_{2(sln,700\,°C)}$	$\Delta H_2 = 60.81^b \pm 0.11^c (401)^d$ [111]
(3)	$Y_2O_{3(s,\,25\,°C)} \rightarrow Y_2O_{3(sln,\,700\,°C)}$	$\Delta H_3 = -120.74 \pm 0.09\,(9)$ [111]
(4)	$Ti_{(s,\,25\,°C)} + O_{2(g,\,25\,°C)} \rightarrow TiO_{2(s,\,rutile,\,25\,°C)}$	$\Delta H_4 = -944.0 \pm 0.8$ [112]
(5)	$2Y_{(s,25\,°C)} + \frac{3}{2}O_{2(g,25\,°C)} \rightarrow Y_2O_{3(s,25\,°C)}$	$\Delta H_5 = -1932.8 \pm 5.2$ [113]
(6)	$H_2O_{(l,\,25\,°C)} \rightarrow H_2O_{(g,\,700\,°C)}$	$\Delta H_6 = 69.00$ [112]
(7)	$H_2O_{(l,\,25\,°C)} \rightarrow H_2O_{(ad,\,25\,°C)}$	$\Delta H_7 = -44.00$ [109]
Corrected ΔH_{ds} for removal of surface adsorbed water		
(8)	$Y_2Ti_2O_{7(s,\,25\,°C)} \rightarrow Y_2O_{3(sln,\,700\,°C)} + TiO_{4(sln,\,700\,°C)} - \Delta H'_{ds} = \Delta H_8 = \Delta H_1 + x(\Delta H_7 - \Delta H_6)$	$\Delta H'_{ds}$
Enthalpy of formation of Y pyrochlore from the oxides		
(9)	$Y_2O_{3(s,\,25\,°C)} + 2TiO_{2(s,\,rutile,25\,°C)} \rightarrow Y_2Ti_2O_{7(s,\,25\,°C)} - \Delta H_{f,\,ox} = \Delta H_9 = -\Delta H_8 + \Delta H_3 + 2\Delta H_2$	$\Delta H_{f,ox}$
Standard enthalpy of formation of Y pyrochlore		
(10)	$2Y_{(s,\,25\,°C)} + 2Ti_{(s,\,25\,°C)} + 7/2O_{2(g,\,25\,°C)} \rightarrow Y_2Ti_2O_{7(s,\,25\,°C)} - \Delta H_f^° = \Delta H_{10} = \Delta H_9 + \Delta H_5 + 2\Delta H_4$	$\Delta H_f^°$

[a] The enthalpies of drop solution, corrected drop solution, formation from the oxides, and formation from the elements are listed in Table S1.† [b] Average. [c] Two standard deviations of the average. [d] Number of measurements.

nanocrystallites by the endothermic signal from 600–900 °C with negligible mass loss at the same temperature.[108]

3.2 Enthalpy of formation of nanosized $Y_2Ti_2O_7$

$Y_2Ti_2O_7$ samples were used in the drop calorimetric experiments without pre-treatment. The thermochemical cycle used for determining the enthalpy of formation of yttrium titanate pyrochlore materials is outlined in Table 2. For nanomaterials, the enthalpy of drop solution (ΔH_{ds}) is the sum of the heat content of the sample, the enthalpy of solution in the oxide-melt solvent, the enthalpy of dehydration of the surface water with its associated heat content, and the excess enthalpy related to the surface.[73] By assuming that all water is physically adsorbed on the surface and is energetically equivalent to liquid water when condensed to solid ice (−44 kJ mol^{-1}),[30,109,110] ΔH_{ds} can be corrected for obtaining the drop solution enthalpy of nanosized $Y_2Ti_2O_7$ with a hydrated surface[30,73,109] ($\Delta H'_{ds}$), further used for deriving $\Delta H_{f,ox}$ and $\Delta H_f^°$ (Table S1†).

All samples in this study were enthalpically favourable to form from the oxides, with $\Delta H_{f,ox}$ positively correlated with surface area (Fig. 3). Insignificant agglomeration was found in three of the sample series and these were used to extrapolate linear trends in energetics, while the sample that deviates from these trends (34 nm) is discussed in-depth in the follow-
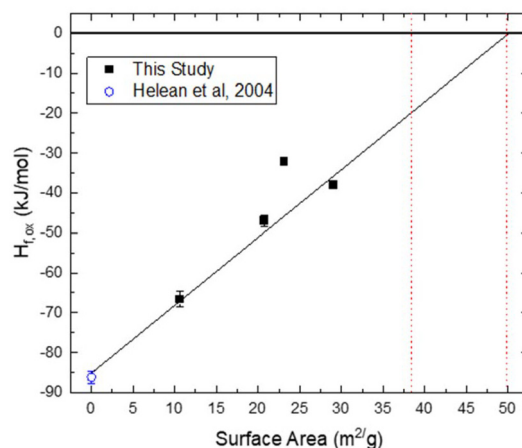

Fig. 3 Calculated enthalpy of formation from the oxides as a function of surface area. *Red vertical dashed lines* indicate the surface area of spherical particles with diameters of 5 to 1.8 nm, where the linear trend of surface enthalpy is not expected to hold. Note the sample with SA = 23 m^2 g^{-1} is not included in the linear trend.

ing sections. Extrapolating the linear trend to the zero enthalpy of formation from the oxides yields a surface area of 50 m^2 g^{-1}, which corresponds to a particle diameter of 1.8 nm (approximately 1.75 unit cell). This suggests that nanosized

$Y_2Ti_2O_7$ smaller than 1.8 nm is thermodynamically metastable and unlikely to form or persist. Although such an implication is based on the hypothesis that physical properties of sub-nano particles still correlate linearly with those of nano-sized and bulk-sized phases, that assumption is sometimes untrue.[61] This is mostly because when the size decreases to below 5 nm (with surface area ~38 m^2 g^{-1}), the percentage of atoms on the surface dominates, which may further cause excess free energy to significantly deviate from the linear trend.[114,115] After all, the linear trend still gives a good estimation in the size that one can use to predict the stability of nanoparticles. On the other hand, as surface area decreases (with increasing particle size), enthalpy of formation from oxides of the nanosized phase typically approaches that of the bulk value. The extrapolated enthalpy value with particle size zero is -85.1 ± 1.6 kJ mol^{-1}, consistent with $\Delta H_{f,ox} = -86.2 \pm 1.5$ kJ mol^{-1} of the bulk-sized $Y_2Ti_2O_7$.[47] Such a good agreement also suggests the high reliability of the size-dependent enthalpy of formation data we measured experimentally.

3.3 Derivation of surface energy from calorimetry

The excess enthalpic contribution to the nanoparticles can be written as

$$\Delta H_{excess} = \Delta H'_{ds}(\text{bulk}) - \Delta H'_{ds}(\text{nano}).$$

In the case of nonaggregated nanoparticles that have negligible interface area, this excess enthalpy directly attributes to the excess energy originated at the termination of the crystal (surface energy, γ)[116] and the total area of the surface of the sample (SA) as

$$\Delta H_{excess} = \gamma \times \text{SA}.$$

In order to derive γ, the corrected drop solution enthalpies were fitted as a linear function of the BET surface area (Fig. 4).[30,110,117] The slope of this line corresponds to the enthalpy of the free particle surface, which was determined to be 4.07 ± 0.32 J m^{-2} ($R^2 = 0.987$). This value agrees well with
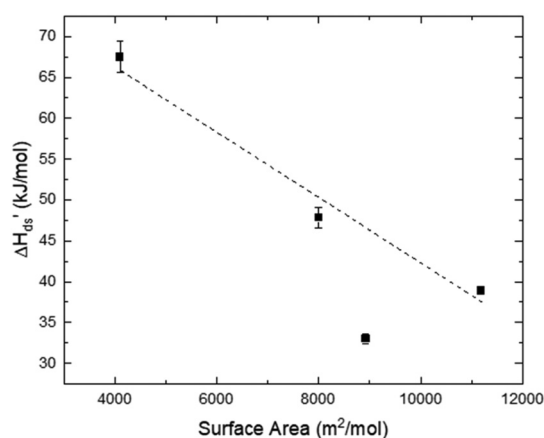
theoretically determined values of the surface energy of titanate pyrochlore materials, as discussed in-depth below. In the case of agglomerated nanoparticles, the grain boundary has additional interfacial energy (γ') that contributes to the excess enthalpy that is proportional to interfacial area (IA).[110,118] Thus, the total excess enthalpy is

$$\Delta H_{excess} = \gamma \times \text{SA} + \gamma' \times \text{IA}.$$

Given that [23 m^2 g^{-1}] has a similar XRD particle diameter to [29 m^2 g^{-1}] but a lower BET surface area, it can be assumed that this sample has significant grain boundaries and additional excess enthalpy that leads to the deviation from the $\Delta H'_{ds}$-SA relationship shown in Fig. 4. If the difference in measured surface area between [23 m^2 g^{-1}] and [29 m^2 g^{-1}] is twice the total interface area of that sample,[110,118] then γ' can be estimated as 3.04 ± 0.70 J m^{-2} for $Y_2Ti_2O_7$ materials.

Previously, surface energies of REE titanate pyrochlores were mostly studied by computational calculations.[119,120] Average surface energies calculated for the specific (100), (110), (111), and (112) planes for REE = Y, Gd, and Lu are summarized in Table 3 with these planes highlighted in the general pyrochlore structure in Fig. 5. The average values of the four

Table 3 Summary of calculated surface energies of pyrochlore material planes

Material	(100)	(110)	(111)	(112)	Average
$Y_2Ti_2O_7$ [119]	3.88 ± 0.51	3.74 ± 0.24	—	—	3.81 ± 0.40
$Gd_2Ti_2O_7$ [120]	4.12 ± 0.25	3.72 ± 0.86	4.07 ± 0.65	3.41 ± 0.13	3.83 ± 0.56
$Lu_2Ti_2O_7$ [120]	4.40 ± 0.08	3.87 ± 0.91	4.04 ± 0.53	3.55 ± 0.09	3.96 ± 0.53

Fig. 4 Corrected enthalpy of drop solution as a function of surface area. Note the sample with SA = 23 m^2 g^{-1} (~9000 m^2 mol^{-1}) is not included in the linear trend.
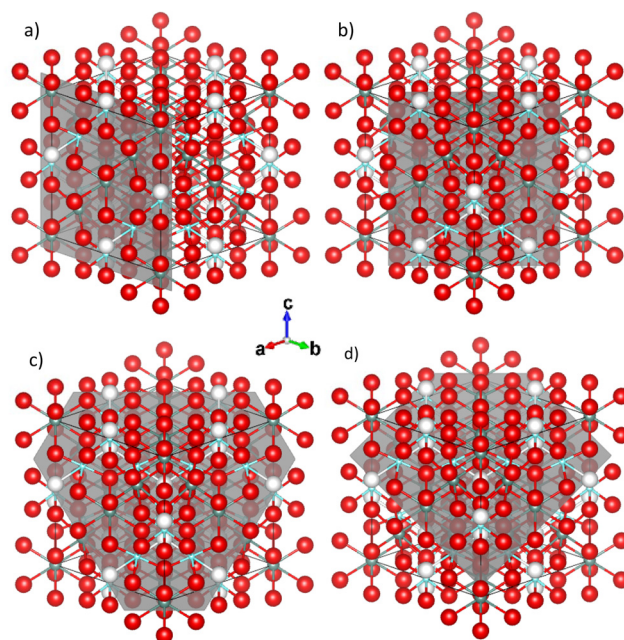

Fig. 5 Perspective view of pyrochlore with lattice planes from computational surface energy studies highlighted. (a) (100); (b) (110); (c) (111); (d) (112).

planes are in excellent agreement with our experimental results. Nanostructures that are not spherical are expected to have a preferential exposure of certain planes to minimize the free energy. The surface energy determined by calorimetry being closer to the high-energy (111) surface instead of the lowest-energy (112) surface indicates the nucleation of these materials by the employed synthetic route as either kinetically controlled or ligand-stabilized instead of thermodynamically driven.

The bulk thermodynamic properties of pyrochlores have been found to be primarily controlled by the incorporated cations. For a given A (or B) cation, there are established trends in the enthalpy of formation from the oxides that can be predicted based on the A/B radius ratio over a range of B (or A) cations.[47,54,121] Cation size also controls nanoscale energetics. For instance, the calculated minimized surface energy of $Gd_2B_2O_7$ (B = Pb, Zr, Hf, Sn, and Ti) has a negative correlation with the ionic size of B cation.[75,120] The most stable surface reported in that study (the (110)-a₁) for $Gd_2Ti_2O_7$ has a surface energy value of ~2.52 J m^{-2}, compared to ~1.87 J m^{-2} for $Gd_2Pb_2O_7$.[120] Also, the average surface energy of $Lu_2Ti_2O_7$ was reported to be higher than that of $La_2Zr_2O_7$ by about 1 J m^{-2}. Because the pyrochlore structure is a derivative of the defect fluorite and fluorite structures, we also summarize surface energy of the latter in Table 4. The B site in pyrochlore is disordered from the defect fluorite with a changed coordination environment from six- to eight-coordinated. With such a change in B site, defect fluorite in general has a small surface energy compared to its pyrochlore counterpart (Table 4). However, within the defect fluorite or fluorite structure, the surface energy increases with increase of cation size, different from the relation seen in pyrochlore that larger B cation suggests smaller surface energy.

3.4 Implication of radiation resistance of nanosized $Y_2Ti_2O_7$

While some data is still unknown for the nanoscale effect on irradiation of pyrochlores, we can create a preliminary lower limit of particle size that should have an increased tolerance to radiation-induced amorphization for the yttrium titanate pyrochlore. The enthalpy of amorphization for $Gd_2Ti_2O_7$ ($\Delta H_{amorphization}$ = 236.6 kJ mol^{-1})[122] $Dy_2Ti_2O_7$ ($\Delta H_{amorphization}$ = 243.3 kJ mol^{-1})[123] and $Dy_2Sn_2O_7$ ($\Delta H_{amorphization}$ = 283.6 kJ mol^{-1})[124] pyrochlores have been experimentally determined.

As this is describing a solid phase system, the entropy contribution to ΔG is considered to be negligible at room temperature or moderately high temperatures. To predict a reasonable $\Delta G_{amorphization}$ value for $Y_2Ti_2O_7$, we correlated the amorphization energy trends with the ionic radii ratio of the pyrochlore compounds (Fig. S8†).

Using this empirical correlation, the amorphization energy of $Y_2Ti_2O_7$ is predicted to be 246.5 ± 4.3 kJ mol^{-1}. Fig. 6 shows this $\Delta G_{amorphization}$ estimate of $Y_2Ti_2O_7$ (black solid line) and the experimentally determined amorphization energy thresholds of two titanium pyrochlores (grey lines). Assuming nanoparticles to be spherical, the contribution from the surfaces to meeting this energy of amorphization can be displayed for many pyrochlore systems as a function of particle diameter. $\Delta G_{surface}$ of $Y_2Ti_2O_7$ (red lines) are average values using the experimentally determined (red solid) and the computationally derived (red dashed) γ values from this study and Yang.[119] The average surface energy is most applicable to spherical nanoparticles as all surfaces are equally exposed, however synthetic methods that tailor synthesis to shapes with a single surface exposed, such as cubes, can minimize the free energy contribution by preferential exposure of the lowest energy surface. A series of cube-shaped gadolinium pyrochlores using the lowest computationally derived surface energy with diameter equal to the length of the side is also shown for comparison in dotted blue lines.[120] These get darker in colour as the size of the B cation decreases.

From Fig. 6, one can estimate that the smallest particle size of $Y_2Ti_2O_7$ that begins to favour crystallinity over amorphization under radiation is approximately 5.0 nm in diameter (considered here as the critical particle size). This is the upper limit of the region one in Fig. 1.[71] With increasing particle size from 5 nm while remaining nanosized, $Y_2Ti_2O_7$ is expected to have enhanced radiation resistance. Furthermore, the effect of the A/B radius ratio on the surface energy contribution can

Table 4 Summary of experimentally determined surface and interface enthalpies of various fluorite-like oxides

Compound	Surface energy (J m^{-2})		Interface energy (J m^{-2})
	Hydrous	Anhydrous	
$Eu_2Zr_2O_7$-df[30]	1.01 ± 0.15	1.47 ± 0.13	
CeO_2-f[110]	0.86 ± 0.02	1.16 ± 0.02	0.81 ± 0.14
ThO_2-f[30]	0.92 ± 0.10	1.21 ± 0.16	
8 mol% YSZ-f[118]	0.85 ± 0.07	1.16 ± 0.08	0.82 ± 0.32
10 mol% YSZ-f[118]	1.04 ± 0.05	1.51 ± 0.20	0.97 ± 0.41
12 mol% YSZ-f[118]	1.27 ± 0.08	1.80 ± 0.13	0.63 ± 0.22

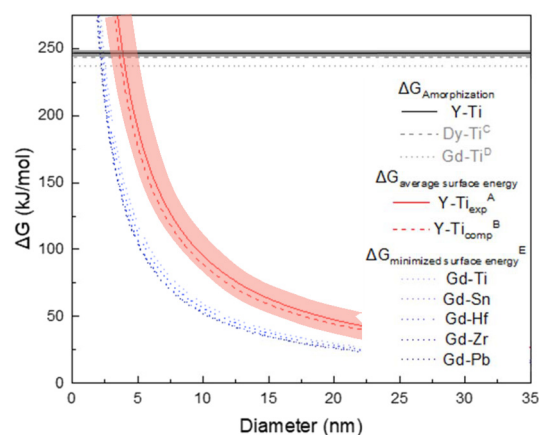df = defect fluorite phase, f = fluorite phase.

Fig. 6 Free energy of amorphization (black) for various pyrochlore compounds and the free energy contribution from the surfaces as a function of particle diameter. Red lines indicate average surface energy and spherical particles, while blue are minimized surface energy of cubic particles. Error envelopes for $Y_2Ti_2O_7$ are indicated by the shaded regions. (A) This study. (B) Yang, 2013.[119] (C) Chung, 2018.[123] (D) Chung, 2019.[122] (E) Dholabhai, 2016.[120]

also be seen in Fig. 6, but it is unknown whether the changes to the amorphization energy decrease at a similar rate as the surface energy for a given composition. Characterization of these radiation resistance effects as trends of cation size will help identify the minimization region of the energetics to be determined, which in turn will allow highly radiation-tolerant pyrochlore nanomaterials to be engineered. On the other hand, the size-dependent defect accumulation in pyrochlore materials has not been sufficiently published at this time to elucidate the ΔG_{defect} contribution which would provide insight into the lower and upper limits of particle diameter in the stable region three, if one exists.

4. Conclusions

Yttrium titanate pyrochlore nanomaterials were synthesized by a modified sol–gel method. The phase crystallinity and particle morphology were confirmed by synchrotron powder X-ray diffraction analysis and transmission electron microscopy, and surface area was determined by BET liquid nitrogen adsorption. Average particle size of samples ranged from 31 nm (29.0 m^2 g^{-1}) to 131 nm (10.6 m^2 g^{-1}) and were loosely spherical in shape. Using high temperature oxide melt drop solution calorimetry, we determined the surface enthalpy for the pyrochlore (4.07 ± 0.32 J m^{-2}) which indicates preferential exposure of the (111) surface, and have estimated interfacial energy (3.04 ± 0.70 J m^{-2}). This information was further used to estimate the critical particle size for Y$_2$Ti$_2$O$_7$ at ~5.0 nm, with smaller particles predicted to spontaneously amorphize or agglomerate. The impact of radiation accumulation and self-healing of nanomaterials was also discussed in this work. It is expected that tunability of exposed particle surfaces for nano-sized ceramic waste hosts will be a key characteristic in the engineering of radiation-resistant materials in the future.

Author contributions

MR and XG conceptualized and designed the study. JW provided samples for the study and collected TEM images. JL and QZ performed the BET experiments and analysed the data. AS collected the XRD data that was analysed by AS and MR. MR and XG performed the high temperature melt drop solution calorimetry and analysed the data. MR and XG interpreted the data. All participated in writing the manuscript.

Conflicts of interest

There are no conflicts to declare.

Acknowledgements

References

1 F. Li, L. Zhou, J. X. Liu, Y. Liang and G. J. Zhang, High-Entropy Pyrochlores with Low Thermal Conductivity for Thermal Barrier Coating Materials, *J. Adv. Ceram.*, 2019, **8**(4), 576–582, DOI: **10.1007/s40145-019-0342-4**.

2 K. Wang, J. Zhu, H. Wang, K. Yang, Y. Zhu, Y. Qing, Z. Ma, L. Gao, Y. Liu, S. Wei, Y. Shu, Y. Zhou and J. He, Air Plasma-Sprayed High-Entropy (Y0.2Yb0.2Lu0.2Eu0.2Er0.2)3Al5O12 Coating with High Thermal Protection Performance, *J. Adv. Ceram.*, 2022, **11**(10), 1571–1582, DOI: **10.1007/s40145-022-0630-2**.

3 S. Zhu, J. Zhu, S. Ye, K. Yang, M. Li, H. Wang and J. He, High-Entropy Rare Earth Titanates with Low Thermal Conductivity Designed by Lattice Distortion, *J. Am. Ceram. Soc.*, 2023, **106**(10), 6279–6291, DOI: **10.1111/jace.19233**.

4 K. Ren, Q. Wang, Y. Cao, G. Shao and Y. Wang, Multicomponent Rare-Earth Cerate and Zirconocerate Ceramics for Thermal Barrier Coating Materials, *J. Eur. Ceram. Soc.*, 2021, **41**(2), 1720–1725, DOI: **10.1016/j.jeurceramsoc.2020.10.005**.

5 D. Chen, Q. Wang, Y. Liu and X. Ning, Microstructure, Thermal Characteristics, and Thermal Cycling Behavior of the Ternary Rare Earth Oxides (La2O3, Gd2O3, and Yb2O3) Co-Doped YSZ Coatings, *Surf. Coat. Technol.*, 2020, **403**, 126387, DOI: **10.1016/j.surfcoat.2020.126387**.

6 J. Sankar and S. S. Kumar, Synthesis of Rare Earth Based Pyrochlore Structured (A2B2O7) Materials for Thermal Barrier Coatings (TBCs)-A Review, in *Current Applied Science and Technology*, King Mongkut's Institute of Technology, Ladkrabang, 2021, pp. 601–617. DOI: **10.14456/cast.2021.47**.

7 M. K. Hossain, M. H. K. Rubel, M. A. Akbar, M. H. Ahmed, N. Haque, M. F. Rahman, J. Hossain and K. M. Hossain, *A Review on Recent Applications and Future Prospects of Rare Earth Oxides in Corrosion and Thermal Barrier Coatings, Catalysts, Tribological, and Environmental Sectors*, Ceramics International. Elsevier Ltd, 2022. DOI: **10.1016/j.ceramint.2022.07.220**.

8 P. E. R. Blanchard, R. Clements, B. J. Kennedy, C. D. Ling, E. Reynolds, M. Avdeev, A. P. J. Stampfl, Z. Zhang and L. Y. Jang, Does Local Disorder Occur in the Pyrochlore Zirconates?, *Inorg. Chem.*, 2012, **51**(24), 13237–13244, DOI: **10.1021/ic301677b**.

9 B. V. Ayodele, M. A. Hossain, S. L. Chong, J. C. Soh, S. Abdullah, M. R. Khan and C. K. Cheng, Non-Isothermal Kinetics and Mechanistic Study of Thermal Decomposition of Light Rare Earth Metal Nitrate Hydrates Using Thermogravimetric Analysis, *J. Therm. Anal. Calorim.*, 2016, **125**(1), 423–435, DOI: **10.1007/s10973-016-5450-6**.

10 A. E. Elkholy, F. E. T. Heakal and W. A. El-Said, Improving the Electrocatalytic Performance of Pd Nanoparticles Supported on Indium/Tin Oxide Substrates towards Glucose Oxidation, *Appl. Catal., A*, 2019, **580**, 28–33, DOI: **10.1016/j.apcata.2019.04.032**.

11 M. T. Behnamfar, H. Hadadzadeh, E. Akbarnejad, A. R. Allafchian, M. Assefi and N. Khedri, Electrocatalytic Reduction of CO2 to CO by Gd(III) and Dy(III) Complexes; And M2O3 Nanoparticles (M = Gd and Dy), *J. CO2 Util.*, 2016, **13**, 61–70, DOI: **10.1016/j.jcou.2015.12.005**.

12 D. R. Rittman, K. M. Turner, S. Park, A. F. Fuentes, J. Yan, R. C. Ewing and W. L. Mao, High-Pressure Behavior of A2B2O7 Pyrochlore (A=Eu, Dy; B=Ti, Zr), *J. Appl. Phys.*, 2017, **121**(4), 045902, DOI: **10.1063/1.4974871**.

13 K. Yang, K. Bryce, W. Zhu, D. Zhao and J. Lian, Multicomponent Pyrochlore Solid Solutions with Uranium Incorporation – A New Perspective of Materials Design for Nuclear Applications, *J. Eur. Ceram. Soc.*, 2021, **41**(4), 2870–2882, DOI: **10.1016/j.jeurceramsoc.2020.12.012**.

14 Q. Wang, H. Fan, Y. Xiao and Y. Zhang, Applications and Recent Advances of Rare Earth in Solid Oxide Fuel Cells, *J. Rare Earths*, 2022, 1668–1681, DOI: **10.1016/j.jre.2021.09.003**. Editorial Office of Chinese Rare Earths.

15 A. P. Anantharaman and H. P. Dasari, *Potential of Pyrochlore Structure Materials in Solid Oxide Fuel Cell Applications*, Ceramics International. Elsevier Ltd, 2021, pp. 4367–4388. DOI: **10.1016/j.ceramint.2020.10.012**.

16 R. S. Kumar, A. L. Cornelius, M. Somayazulu, D. Errandonea, M. F. Nicol and J. Gardner, High Pressure Structure of Tb2Ti2O7 Pyrochlore at Cryogenic Temperatures, *Phys. Status Solidi B*, 2007, **244**(1), 266–269, DOI: **10.1002/pssb.200672558**.

17 M. Lang, F. Zhang, J. Zhang, J. Wang, J. Lian, W. J. Weber, B. Schuster, C. Trautmann, R. Neumann and R. C. Ewing, Review of A2B2O7 Pyrochlore Response to Irradiation and Pressure, *Nucl. Instrum. Methods Phys. Res., Sect. B*, 2010, **268**(19), 2951–2959, DOI: **10.1016/j.nimb.2010.05.016**.

18 J. K. Gill, O. P. Pandey and K. Singh, Role of Sintering Temperature on Thermal, Electrical and Structural Properties of Y2Ti2O7 Pyrochlores, *Int. J. Hydrogen Energy*, 2011, **36**(22), 14943–14947, DOI: **10.1016/j.ijhydene.2011.02.138**.

19 D. J. Gregg, Y. Zhang, S. C. Middleburgh, S. D. Conradson, G. Triani, G. R. Lumpkin and E. R. Vance, The Incorporation of Plutonium in Lanthanum Zirconate Pyrochlore, *J. Nucl. Mater.*, 2013, **443**(1–3), 444–451, DOI: **10.1016/j.jnucmat.2013.07.030**.

20 T. Ringwood, Immobilization of Radioactive Wastes in SYNROC, *Am. Sci.*, 1982, **70**(2), 201–207.

21 W. Sinclair and A. E. Ringwood, Alpha-Recoil Damage in Natural Zirconolite and Perovskite, *Geochem. J.*, 1981, **15**(5), 229–243, DOI: **10.2343/geochemj.15.229**.

22 W. J. Weber, R. C. Ewing, C. A. Angell, G. W. Arnold, A. N. Cormack, J. M. Delaye, D. L. Griscom, L. W. Hobbs, A. Navrotsky, D. L. Price, A. M. Stoneham and M. C. Weinberg, Radiation Effects in Glasses Used for Immobilization of High-Level Waste and Plutonium Disposition, *J. Mater. Res.*, 1997, **12**(8), 1948–1978, DOI: **10.1557/jmr.1997.0266**.

23 W. J. Weber, A. Navrotsky, S. Stefanovsky, E. R. Vance and E. Vernaz, Materials Science of High-Level Nuclear Waste Immobilization, *MRS Bull.*, 2009, **34**(1), DOI: **10.1557/mrs2009.12**.

24 B. E. Burakov, E. B. Anderson, D. A. Knecht, M. A. Zamoryanskaya, E. E. Strykanova and M. A. Yagovkina, Synthesis of Garnet/Perovskite-Based Ceramic for the Immobilization of Pu-Residue Wastes. In *Materials Research Society Symposium - Proceedings*, 1999, Vol. 556. DOI: **10.1557/proc-556-55**.

25 S. V. Yudintsev, M. I. Lapina, A. G. Ptashkin, T. S. Ioudintseva, S. Utsunomiya, L. M. Wang and R. C. Ewing, Accommodation of Uranium into the Garnet Structure, *Mater. Res. Soc. Symp. Proc.*, 2002, **713**, JJ11-28, DOI: **10.1557/proc-713-jj11.28**.

26 S. V. Yudintsev, S. V. Stefanovsky and R. C. Ewing, Actinide Host Phases as Radioactive Waste Forms, in *Structural Chemistry of Inorganic Actinide Compounds*, 2007. DOI: **10.1016/B978-044452111-8/50014-4**.

27 G. R. Lumpkin, Ceramic Waste Forms for Actinides, *Elements*, 2006, **2**(6), 365–372, DOI: **10.2113/gselements.2.6.365**.

28 C. Nästren, R. Jardin, J. Somers, M. Walter and B. Brendebach, Actinide Incorporation in a Zirconia Based Pyrochlore (Nd1.8An0.2)Zr2O7 + x (An=Th, U, Np, Pu, Am), *J. Solid State Chem.*, 2009, **182**(1), 1–7, DOI: **10.1016/j.jssc.2008.09.017**.

29 Z. Tang, Z. Huang, W. Han, J. Qi, Y. Shi, N. Ma, Y. Zhang, X. Guo and T. Lu, Uranium-Incorporated Pyrochlore La2(UxMgxZr1–2 x)2O7Nuclear Waste Form: Structure and Phase Stability, *Inorg. Chem.*, 2020, **59**(14), 9919–9926, DOI: **10.1021/acs.inorgchem.0c01089**.

30 M. P. Saradhi, S. V. Ushakov and A. Navrotsky, Fluorite-Pyrochlore Transformation in Eu 2Zr 2O 7 - Direct Calorimetric Measurement of Phase Transition, Formation and Surface Enthalpies, *RSC Adv.*, 2012, **2**(8), 3328–3334, DOI: **10.1039/c2ra00727d**.

31 P. Li, I.-W. Chen and J. E. Penner–Hahn, Effect of Dopants on Zirconia Stabilization—An X–ray Absorption Study: II, Tetravalent Dopants, *J. Am. Ceram. Soc.*, 1994, **77**(5), 1281–1288, DOI: **10.1111/j.1151-2916.1994.tb05403.x**.

32 W. J. Weber, R. C. Ewing, C. R. A. Catlow, T. Diaz De La Rubia, L. W. Hobbs, C. Kinoshita, H. Matzke, A. T. Motta, M. Nastasi, E. K. H. Salje, E. R. Vance and S. J. Zinkle, Radiation Effects in Crystalline Ceramics for the Immobilization of High-Level Nuclear Waste and Plutonium, *J. Mater. Res.*, 1998, **13**(6), 1434–1484, DOI: **10.1557/JMR.1998.0205**.

33 R. B. Greegor, F. W. Lytle, R. J. Livak and F. W. Clinard, X-Ray Spectroscopic Investigation of Pu-Substituted Zirconolite, *J. Nucl. Mater.*, 1988, **152**(2–3), 270–277, DOI: **10.1016/0022-3115(88)90336-4**.

34 M. Abdou, S. K. Gupta, J. P. Zuniga and Y. Mao, On Structure and Phase Transformation of Uranium Doped La2Hf2O7 Nanoparticles as an Efficient Nuclear Waste Host, *Mater. Chem. Front.*, 2018, **2**(12), 2201–2211, DOI: **10.1039/c8qm00266e**.

35 J. Shamblin, M. Feygenson, J. Neuefeind, C. L. Tracy, F. Zhang, S. Finkeldei, D. Bosbach, H. Zhou, R. C. Ewing and M. Lang, Probing Disorder in Isometric Pyrochlore and Related Complex Oxides, *Nat. Mater.*, 2016, **15**(5), 507–511, DOI: **10.1038/nmat4581**.

36 D. L. Drey, E. C. O'Quinn, T. Subramani, K. Lilova, G. Baldinozzi, I. M. Gussev, A. F. Fuentes, J. C. Neuefeind, M. Everett, D. Sprouster, A. Navrotsky, R. C. Ewing and M. Lang, Disorder in Ho2Ti2−xZrxO7: Pyrochlore to Defect Fluorite Solid Solution Series, *RSC Adv.*, 2020, **10**(57), 34632–34650, DOI: **10.1039/d0ra07118h**.

37 J. M. Solomon, J. Shamblin, M. Lang, A. Navrotsky and M. Asta, Chemical Ordering in Substituted Fluorite Oxides: A Computational Investigation of Ho2 Zr2 O7 and RE2 Th2 O7 (RE=Ho, Y, Gd, Nd, La), *Sci. Rep.*, 2016, **6**, 1–10, DOI: **10.1038/srep38772**.

38 M. A. Subramanian, G. Aravamudan and G. V. Subba Rao, Oxide, Pyrochlores - A Review, *Prog. Solid State Chem.*, 1983, **15**(2), 55–143, DOI: **10.1016/0079-6786(83)90001-8**.

39 R. C. Ewing, W. J. Weber and J. Lian, Nuclear Waste Disposal-Pyrochlore (A 2B 2O 7): Nuclear Waste Form for the Immobilization of Plutonium and "Minor" Actinides, *J. Appl. Phys.*, 2004, **95**(11 I), 5949–5971, DOI: **10.1063/1.1707213**.

40 Y. F. Volkov, S. V. Tomilin, A. N. Lukinykh, A. A. Lizin, A. A. Elesin, A. G. Yakovenko, V. I. Spiryakov, A. V. Bychkov and L. J. Jardine, Titanate Ceramics with Pyrochlore Structure as a Matrix for Immobilization of Excess Weapons-Grade Plutonium: I. Radiation Resistance, *Radiochemistry*, 2004, **46**(4), 322–328, DOI: **10.1023/B:RACH.0000039111.16794.e8**.

41 S. Finkeldei, M. C. Stennett, P. M. Kowalski, Y. Ji, E. De Visser-Týnová, N. C. Hyatt, D. Bosbach and F. Brandt, Insights into the Fabrication and Structure of Plutonium Pyrochlores, *J. Mater. Chem. A*, 2020, **8**(5), 2387–2403, DOI: **10.1039/c9ta05795a**.

42 R. C. Ewing, B. C. Chakoumakos, G. R. Lumpkin, T. Murakami, R. B. Greegor and F. W. Lytle, Metamict Minerals: Natural Analogues for Radiation Damage Effects in Ceramic Nuclear Waste Forms, *Nucl. Instrum. Methods Phys. Res., Sect. B*, 1988, **32**(1–4), 487–497, DOI: **10.1016/0168-583X(88)90259-5**.

43 B. D. Wirth, How Does Radiation Damage Materials?, *Science*, 2007, **318**(5852), 923–924, DOI: **10.1126/science.1150394**.

44 S. J. Zinkle and K. Farrell, Void Swelling and Defect Cluster Formation in Reactor-Irradiated Copper, *J. Nucl. Mater.*, 1989, **168**(3), 262–267, DOI: **10.1016/0022-3115(89)90591-6**.

45 J. Wen, C. Sun, P. P. Dholabhai, Y. Xia, M. Tang, D. Chen, D. Y. Yang, Y. H. Li, B. P. Uberuaga and Y. Q. Wang, Temperature Dependence of the Radiation Tolerance of Nanocrystalline Pyrochlores A2Ti2O7 (A = Gd, Ho and Lu), *Acta Mater.*, 2016, **110**, 175–184, DOI: **10.1016/j.actamat.2016.03.025**.

46 H. Zhao, X. Zeng, X. Yang, W. Chen and J. Wu, Investigation of the Temperature Effect on the Primary Radiation Damage Near the Grain Boundary in Tungsten Using Molecular Dynamics Simulations, *Nucl. Instrum. Methods Phys. Res., Sect. B*, 2020, **476**, 32–39, DOI: **10.1016/j.nimb.2020.04.030**.

47 K. B. Helean, S. V. Ushakov, C. E. Brown, A. Navrotsky, J. Lian, R. C. Ewing, J. M. Farmer and L. A. Boatner, Formation Enthalpies of Rare Earth Titanate Pyrochlores, *J. Solid State Chem.*, 2004, **177**(6), 1858–1866, DOI: **10.1016/j.jssc.2004.01.009**.

48 J. Lian, L. M. Wang, R. C. Ewing and L. A. Boatner, Ion Beam Implantation and Cross-Sectional TEM Studies of Lanthanide Titanate Pyrochlore Single Crystals, *Nucl. Instrum. Methods Phys. Res., Sect. B*, 2005, **241**(1–4), 365–371, DOI: **10.1016/j.nimb.2005.07.043**.

49 B. D. Begg, N. J. Hess, W. J. Weber, R. Devanathan, J. P. Icenhower, S. Thevuthasan and B. P. McGrail, Heavy-Ion Irradiation Effects on Structures and Acid Dissolution of Pyrochlores, *J. Nucl. Mater.*, 2001, **288**(2–3), 208–216, DOI: **10.1016/S0022-3115(00)00708-X**.

50 S. X. Wang, B. D. Begg, L. M. Wang, R. C. Ewing, W. J. Weber and K. V. Govidan Kutty, Radiation Stability of Gadolinium Zirconate: A Waste Form for Plutonium Disposition, *J. Mater. Res.*, 1999, **14**(12), 4470–4473, DOI: **10.1557/JMR.1999.0606**.

51 J. Lian, X. T. Zu, K. V. G. Kutty, J. Chen, L. M. Wang, R. C. Ewing and R. C. Ewing, Ion-Irradiation-Induced Amorphization of La2Zr2O7 Pyrochlore, *Phys. Rev. B: Condens. Matter Mater. Phys.*, 2002, **66**(5), 541081–541085, DOI: **10.1103/PhysRevB.66.054108**.

52 K. E. Sickafus, R. W. Grimes, J. A. Valdez, A. Cleave, M. Tang, M. Ishimaru, S. M. Corish, C. R. Stanek and B. P. Uberuaga, Radiation-Induced Amorphization Resistance and Radiation Tolerance in Structurally Related Oxides, *Nat. Mater.*, 2007, **6**(3), 217–223, DOI: **10.1038/nmat1842**.

53 J. Lian, J. Chen, M. Wang, R. C. Ewing, J. M. Farmer, L. A. Boatner and B. Helean, Radiation-Induced Amorphization of Rare-Earth Titanate Pyrochlores, *Phys. Rev. B: Condens. Matter Mater. Phys.*, 2003, **68**(13), 1–9, DOI: **10.1103/PhysRevB.68.134107**.

54 J. Lian, K. B. Helean, B. J. Kennedy, L. M. Wang, A. Navrotsky and R. C. Ewing, Effect of Structure and Thermodynamic Stability on the Response of Lanthanide Stannate Pyrochlores to Ion Beam Irradiation, *J. Phys. Chem. B*, 2006, **110**(5), 2343–2350, DOI: **10.1021/jp055266c**.

55 J. Lian, L. M. Wang, S. X. Wang, J. Chen, L. A. Boatner and R. C. Ewing, Nanoscale Manipulation of Pyrochlore: New Nanocomposite Ionic Conductors, *Phys. Rev. Lett.*, 2001, **87**(14), 3–6, DOI: **10.1103/PhysRevLett.87.145901**.

56 J. Zhang, J. Lian, A. F. Fuentes, F. Zhang, M. Lang, F. Lu and R. C. Ewing, Enhanced Radiation Resistance of Nanocrystalline Pyrochlore Gd2 (Ti0.65 Zr0.35) 2 O7, *Appl. Phys. Lett.*, 2009, **94**(24), 14–16, DOI: **10.1063/1.3155855**.

57 R. A. Andrievski, BEHAVIOR OF RADIATION DEFECTS IN NANOMATERIALS, *Rev. Adv. Mater. Sci.*, 2011, **29**, 54–67.

58 X. M. Bai, A. F. Voter, R. G. Hoagland, M. Nastasi and B. P. Uberuaga, Efficient Annealing of Radiation Damage near Grain Boundaries via Interstitial Emission, *Science*, 2010, **327**(5973), 1631–1634, DOI: **10.1126/science.1183723**.

59 G. Ackland, Controlling Radiation Damage, *Science*, 2010, **327**, 1587–1588, DOI: **10.1126/science.1188088**.

60 L. Xu, H. W. Liang, Y. Yang and S. H. Yu, Stability and Reactivity: Positive and Negative Aspects for Nanoparticle Processing, *Chem. Rev.*, 2018, **118**(7), 3209–3250, DOI: **10.1021/acs.chemrev.7b00208**.

61 D. Prieur, W. Bonani, K. Popa, O. Walter, K. W. Kriegsman, M. H. Engelhard, X. Guo, R. Eloirdi, T. Gouder, A. Beck, T. Vitova, A. C. Scheinost, K. Kvashnina and P. Martin, Size Dependence of Lattice Parameter and Electronic Structure in CeO_2 Nanoparticles, *Inorg. Chem.*, 2020, **59**(8), 5760–5767, DOI: **10.1021/acs.inorgchem.0c00506**.

62 A. Navrotsky, Energetics at the Nanoscale: Impacts for Geochemistry, the Environment, and Materials, *MRS Bull.*, 2016, **41**(2), 139–145, DOI: **10.1557/mrs.2015.336**.

63 S. Zhang and L. Chen, Thermodynamic Stability of Nanoparticles Based on Coordination Number, *Nanomater. Energy*, 2018, **7**(2), 26–31, DOI: **10.1680/jnaen.18.00001**.

64 R. H. R. Castro, On the Thermodynamic Stability of Nanocrystalline Ceramics, *Mater. Lett.*, 2013, **96**, 45–56, DOI: **10.1016/j.matlet.2013.01.007**.

65 W. Li, Z. Cui, H. Duan and Y. Xue, Effect of Nanoparticle Size on the Thermal Decomposition Thermodynamics in Theory and Experiment, *Appl. Phys. A: Mater. Sci. Process.*, 2016, **122**(2), 1–12, DOI: **10.1007/s00339-016-9609-6**.

66 L. Cademartiri, G. Ozin and J. Lehn, *Concepts of Nanochemistry*, American Library Association, 2009.

67 R. A. Andrievski, The Role of Interfaces in Nanomaterials Behavior at Extremes, *Diffus. Found.*, 2015, **5**, 147–170, DOI: **10.4028/www.scientific.net/DF.5.147**.

68 I. J. Beyerlein, M. J. Demkowicz, A. Misra and B. P. Uberuaga, Defect-Interface Interactions., *Prog. Mater. Sci.*, 2015, **74**, 125–210, DOI: **10.1016/j.pmatsci.2015.02.001**.

69 S. Wurster and R. Pippan, Nanostructured Metals under Irradiation, *Scr. Mater.*, 2009, **60**(12), 1083–1087, DOI: **10.1016/j.scriptamat.2009.01.011**.

70 C. Jiang, N. Swaminathan, J. Deng, D. Morgan and I. Szlufarska, Effect of Grain Boundary Stresses on Sink

Strength, *Mater. Res. Lett.*, 2014, **2**(2), 100–106, DOI: **10.1080/21663831.2013.871588**.

71 T. D. Shen, Radiation Tolerance in a Nanostructure: Is Smaller Better?, *Nucl. Instrum. Methods Phys. Res., Sect. B*, 2008, **266**(6), 921–925, DOI: **10.1016/j.nimb.2008.01.039**.

72 S. Dey, J. W. Drazin, Y. Wang, J. A. Valdez, T. G. Holesinger, B. P. Uberuaga and R. H. R. R. Castro, Radiation Tolerance of Nanocrystalline Ceramics: Insights from Yttria Stabilized Zirconia, *Sci. Rep.*, 2015, **5**, 1–9, DOI: **10.1038/srep07746**.

73 A. Navrotsky, Nanoscale Effects on Thermodynamics and Phase Equilibria in Oxide Systems, *ChemPhysChem*, 2011, **12**, 2207–2215, DOI: **10.1002/cphc.201100129**.

74 K. R. Long, B. S. Van Gosen, N. K. Foley and D. Cordier, *The Principal Rare Earth Elements Deposits of the United States—A Summary of Domestic Deposits and a Global Perspective Gd Pr Sm Nd La Ce*, 2010.

75 R. D. Shannon, Revised Effective Ionic Radii and Systematic Studies of Interatomic Distances in Halides and Chalcogenides, *Acta Crystallogr., Sect. A: Cryst. Phys., Diffr., Theor. Gen. Crystallogr.*, 1976, **32**(5), 751–767, DOI: **10.1107/S0567739476001551**.

76 J. Wang, R. C. Ewing and U. Becker, Defect Formation Energy in Pyrochlore: The Effect of Crystal Size, *Mater. Res. Express*, 2014, **1**(3), 035501, DOI: **10.1088/2053-1591/1/3/035501**.

77 F. X. Zhang, J. Lian, J. M. Zhang, K. J. Moreno, A. F. Fuentes, Z. Wang and R. C. Ewing, Increased Stability of Nanocrystals of Gd2(Ti0.65Zr0.35)2O7 Pyrochlore at High Pressure, *J. Alloys Compd.*, 2010, **494**(1–2), 34–39, DOI: **10.1016/j.jallcom.2010.01.036**.

78 S. J. McCormack and A. Navrotsky, Thermodynamics of High Entropy Oxides, *Acta Mater.*, 2021, **202**, 1–21, DOI: **10.1016/j.actamat.2020.10.043**.

79 J. D. Ault and A. J. E. Welch, The Yttrium Oxide - Titanium Dioxide System, *Acta Crystallogr.*, 1966, **20**, 410–412.

80 A. L. Hector and S. B. Wiggin, Synthesis and Structural Study of Stoichiometric Bi2Ti 2O7 Pyrochlore, *J. Solid State Chem.*, 2004, **177**(1), 139–145, DOI: **10.1016/S0022-4596(03)00378-5**.

81 K. W. Li, H. Wang and H. Yan, Hydrothermal Preparation and Photocatalytic Properties of Y2Sn2O7 Nanocrystals, *J. Mol. Catal. A: Chem.*, 2006, **249**(1–2), 65–70, DOI: **10.1016/j.molcata.2006.01.002**.

82 Z. Tang, L. Zhou, L. Yang and F. Wang, A Study on the Structure Transformation and Luminescence of Eu(III) Titanate Nanotubes Synthesized at Various Hydrothermal Temperatures, *J. Alloys Compd.*, 2009, **481**(1–2), 704–709, DOI: **10.1016/j.jallcom.2009.03.077**.

83 K. M. Lin, C. C. Lin, C. Y. Hsiao and Y. Y. Li, Synthesis of Gd2Ti2O7:Eu3+, V4+ Phosphors by Sol-Gel Process and Its Luminescent Properties, *J. Lumin.*, 2007, **127**(2), 561–567, DOI: **10.1016/j.jlumin.2007.03.010**.

84 S. E. Shirsath, D. Wang, S. S. Jadhav, M. L. Mane and S. Li, Ferrites Obtained by Sol-Gel Method, in *Handbook of*

Sol-Gel Science and Technology: Processing, Characterization and Applications, Springer International Publishing, 2018, pp. 695–735. DOI: **10.1007/978-3-319-32101-1_125**.

85   Z. S. Chen, W. P. Gong, T. F. Chen and S. L. Li, *Synthesis and Characterization of Pyrochlore-Type Yttrium Titanate Nanoparticles by Modified Sol-Gel Method*, 2011, Vol. 34.

86   Y. Zhang, M. Wang, Z. Le, G. Huang, L. Zou and Z. Chen, Preparation and Characterization of Pyrochlore Oxide Y2Ti 2O7 Nanocrystals via Gel-Combustion Route, *Ceram. Int.*, 2014, **40**(4), 5223–5230, DOI: **10.1016/j. ceramint.2013.10.091**.

87   R. F. Ali, J. S. Ovens, K. Starosta and B. D. Gates, Novel Defect-Fluorite Pyrochlore Sodium Niobate Nanoparticles: Solution-Phase Synthesis and Radiation Tolerance Analysis, *Nanoscale*, 2019, **11**(12), 5489–5498, DOI: **10.1039/c8nr10385b**.

88   S. Verma, S. Rani and S. Kumar, Crystal Structure Morphology and Optical Behaviour of Sol-Gel Derived Pyrochlore Rare Earth Titanates RE2Ti2O7 (RE=Dy, Sm), *J. Alloys Compd.*, 2018, **750**, 902–910, DOI: **10.1016/j. jallcom.2018.04.110**.

89   L. Kong, I. Karatchevtseva, R. D. Aughterson, J. Davis, Y. Zhang, G. R. Lumpkin and G. Triani, New Pathway for the Preparation of Pyrochlore Nd2Zr2O7 Nanoparticles, *Ceram. Int.*, 2015, **41**(6), 7618–7625, DOI: **10.1016/j. ceramint.2015.02.087**.

90   B. H. Toby and R. B. Von Dreele, GSAS-II: The Genesis of a Modern Open-Source All Purpose Crystallography Software Package, *J. Appl. Crystallogr.*, 2013, **46**(2), 544–549, DOI: **10.1107/S0021889813003531**.

91   A. C. Strzelecki, C. Bourgeois, K. W. Kriegsman, P. Estevenon, N. Wei, S. Szenknect, A. Mesbah, D. Wu, R. C. Ewing, N. Dacheux and X. Guo, Thermodynamics of CeSiO4 : Implications for Actinide Orthosilicates, *Inorg. Chem.*, 2020, **59**(18), 13174–13183, DOI: **10.1021/acs. inorgchem.0c01476**.

92   A. C. Strzelecki, Y. Ren, S. Chong, B. J. Riley, H. Xu, J. S. Mccloy and X. Guo, Structure and Thermodynamics of Calcium Rare Earth Silicate Oxyapatites, Ca2RE8(SiO4) 6O2 (RE=Pr, Tb, Ho, Tm), *Phys. Chem. Miner.*, 2022, **49**(5), 1–13, DOI: **10.1007/s00269-022-01187-5**.

93   A. C. Strzelecki, T. Barral, P. Estevenon, A. Mesbah, V. Goncharov, J. Baker, J. Bai, N. Clavier, S. Szenknect, A. Migdisov, H. Xu, R. C. Ewing, N. Dacheux and X. Guo, The Role of Water and Hydroxyl Groups in the Structures of Stetindite and Coffinite, MSiO4 (M=Ce, U), *Inorg. Chem.*, 2021, **60**(2), 718–735, DOI: **10.1021/acs. inorgchem.0c02757**.

94   H. Xu, M. E. Chavez, J. N. Mitchell, T. J. Garino, H. L. Schwarz, M. A. Rodriguez, D. X. Rademacher and T. M. Nenoff, Crystal Structure and Thermodynamic Stability of Ba/Ti–Substituted Pollucites for Radioactive Cs/Ba Immobilization, *J. Am. Ceram. Soc.*, 2015, **98**(8), 2634–2640, DOI: **10.1111/jace.13608.**

95   X. Guo, X. Lü, J. T. White, C. J. Benmore, A. T. Nelson, R. C. Roback and H. Xu, Bulk Moduli and High Pressure

Crystal Structure of U3Si2, *J. Nucl. Mater.*, 2019, **523**, 135–142, DOI: **10.1016/j.jnucmat.2019.06.006**.

96   A. C. Strzelecki, K. Kriegsman, P. Estevenon, V. Goncharov, J. Bai, S. Szenknect, A. Mesbah, D. Wu, J. S. Mccloy, N. Dacheux and X. Guo, High-Temperature Thermodynamics of Cerium Silicates, A-Ce2Si2O7, and Ce4.67(SiO4)3O, *ACS Earth Space Chem.*, 2020, **4**(11), 2129–2143, DOI: **10.1021/acsearthspacechem.0c00231**.

97   V. G. Goncharov, H. Nisbet, A. Strzelecki, C. J. Benmore, A. A. Migdisov, H. Xu and X. Guo, Energetics of Hydroxylbastnäsite Solid Solutions, La1−xNdxCO3OH, *Geochim. Cosmochim. Acta*, 2022, **330**, 47–66, DOI: **10.1016/j.gca.2022.04.002**.

98   A. C. Strzelecki, M. Reece, X. Zhao, W. Yu, C. Benmore, Y. Ren, C. Alcorn, A. Migdisov, H. Xu and X. Guo, Crystal Chemistry and Thermodynamics of HREE (Er, Yb) Mixing in a Xenotime Solid Solution, *ACS Earth Space Chem.*, 2022, **6**(5), 1375–1389, DOI: **10.1021/ acsearthspacechem.2c00052**.

99   S. Karcher, T. Olds, M. Weber, C. Corkhill, K. Kriegsman, X. Zhao, D. Field and J. Mccloy, Benefits of Using Multiple Raman Laser Wavelengths for Characterizing Defects in a UO 2 Matrix, *J. Raman Spectrosc.*, 2022, 988–1002, DOI: **10.1002/jrs.6321**.

100 T. A. Olds, S. E. Karcher, K. W. Kriegsman, X. Guo and J. S. Mccloy, Oxidation and Anion Lattice Defect Signatures of Hypostoichiometric, *J. Nucl. Mater.*, 2020, **530**, 151959, DOI: **10.1016/j.jnucmat.2019.151959**.

101 K. B. Helean, A. Navrotsky, E. R. Vance, M. L. Carter, B. Ebbinghaus, O. Krikorian, J. Lian, L. M. Wang and J. G. Catalano, Enthalpies of Formation of Ce-Pyrochlore, Ca0.93Ce1.00Ti2.035O7.00, U-Pyrochlore, Ca1.46U4 + 0.23U6 + 0.46Ti1.85O7.00 and Gd-Pyrochlore, Gd2Ti2O7: Three Materials Relevant to the Proposed Waste Form for Excess Weapons Plutonium, *J. Nucl. Mater.*, 2002, **303**(2–3), 226–239, DOI: **10.1016/s0022-3115(02)00795-x**.

102 X. Guo, S. Szenknect, A. Mesbah, S. Labs, N. Clavier, C. Poinssot, S. V. Ushakov, H. Curtius, D. Bosbach, R. C. Ewing, P. C. Burns, N. Dacheux and A. Navrotsky, Thermodynamics of Formation of Coffinite, USiO4, *Proc. Natl. Acad. Sci. U. S. A.*, 2015, **112**(21), 6551–6555, DOI: **10.1073/pnas.1507441112**.

103 F. A. Mumpton and R. Roy, Hydrothermal Stability Studies of the Zircon-Thorite Group, *Geochim. Cosmochim. Acta*, 1961, **21**(3–4), 217–228, DOI: **10.1016/s0016-7037(61) 80056-2**.

104 D. Gorman-Lewis, L. Mazeina, J. B. Fein, J. E. S. Szymanowski, P. C. Burns and A. Navrotsky, Thermodynamic Properties of Soddyite from Solubility and Calorimetry Measurements, *J. Chem. Thermodyn.*, 2007, **39**(4), 568–575, DOI: **10.1016/j.jct.2006.09.005**.

105 A. Navrotsky, T. Shvareva and X. Guo, Thermodynamics of Uranium Minerals and Related Materials, *Mineral. Assoc. Can.*, 2013, **43**, 147–164.

106 X. Guo, E. Tiferet, L. Qi, J. M. Solomon, A. Lanzirotti, M. Newville, M. H. Engelhard, R. K. Kukkadapu, D. Wu,

E. S. Ilton, M. Asta, S. R. Sutton, H. Xu and A. Navrotsky, U(v) in Metal Uranates: A Combined Experimental and Theoretical Study of MgUO4, CrUO4, and FeUO4, *Dalton Trans.*, 2016, **45**(11), 4622–4632, DOI: **10.1039/c6dt00066e**.

107 X. Guo, D. Wu, H. Xu, P. C. Burns and A. Navrotsky, Thermodynamic Studies of Studtite Thermal Decomposition Pathways via Amorphous Intermediates UO3, U2O7, and UO4, *J. Nucl. Mater.*, 2016, **478**, 158–163, DOI: **10.1016/j.jnucmat.2016.06.014**.

108 R. Patakfalvi and I. Dékány, Nucleation and Growth of Silver Nanoparticles Monitored by Titration Microcalorimetry, *J. Therm. Anal. Calorim.*, 2005, **79**(3), 587–594, DOI: **10.1007/s10973-005-0583-z**.

109 S. V. Ushakov and A. Navrotsky, Direct Measurements of Water Adsorption Enthalpy on Hafnia and Zirconia, *Appl. Phys. Lett.*, 2005, **87**(16), 1–3, DOI: **10.1063/1.2108113**.

110 S. Hayun, T. Y. Shvareva and A. Navrotsky, Nanoceria-Energetics of Surfaces, Interfaces and Water Adsorption, *J. Am. Ceram. Soc.*, 2011, **94**(11), 3992–3999, DOI: **10.1111/j.1551-2916.2011.04648.x**.

111 A. Navrotsky, Progress and New Directions in Calorimetry: A 2014 Perspective, *J. Am. Ceram. Soc.*, 2014, **97**(11), 3349–3359, DOI: **10.1111/jace.13278**.

112 R. Robie and B. S. Hemingway, Thermodynamic Properties of Minerals and Related Substances at 298.15K and 1 Bar, *U.S. Geol. Surv. Bull.*, 1995, 1–461.

113 L. R. Morss, Chapter 122 Comparative Thermochemical and Oxidation-Reduction Properties of Lanthanides and Actinides, in *Lanthanides/Actinides: Chemistry; Handbook on the Physics and Chemistry of Rare Earths*, Elsevier, 1994, vol. 18, pp. 239–291. DOI: **10.1016/S0168-1273(05)80045-5**.

114 B. H. Kim, M. J. Hackett, J. Park and T. Hyeon, Synthesis, Characterization, and Application of Ultrasmall Nanoparticles, *Chem. Mater.*, 2014, **26**(1), 59–71, DOI: **10.1021/cm402225z**.

115 C. Nutzenadel, A. Zuttel, D. Chartouni, G. Schmid and L. Schlapbach, Critical Size and Surface Effect of the Hydrogen Interaction of Palladium Clusters, *Eur. Phys. J. D*, 2000, **8**, 245–250, DOI: **10.1007/s100530050033**.

116 F. D. Fischer, T. Waitz, D. Vollath and N. K. Simha, On the Role of Surface Energy and Surface Stress in Phase-Transforming Nanoparticles, *Prog. Mater. Sci.*, 2008, **53**(3), 481–527, DOI: **10.1016/j.pmatsci.2007.09.001**.

117 S. Hayun, S. V. Ushakov and A. Navrotsky, Direct Measurement of Surface Energy of CeO_2 by Differential Scanning Calorimetry, *J. Am. Ceram. Soc.*, 2011, **94**(11), 3679–3682, DOI: **10.1111/j.1551-2916.2011.04843.x**.

118 G. C. C. Costa, S. V. Ushakov, R. H. R. Castro, A. Navrotsky and R. Muccillo, Calorimetric Measurement of Surface and Interface Enthalpies of Yttria-Stabilized Zirconia (YSZ), *Chem. Mater.*, 2010, **22**(9), 2937–2945, DOI: **10.1021/cm100255u**.

119 L. Yang, Y. Jiang, G. R. Odette and W. Zhou, Nonstoichiometry and Relative Stabilities of Y 2 Ti 2 O 7 Polar Surfaces : A Density Functional Theory Prediction, *Acta Mater.*, 2013, **61**(19), 7260–7270, DOI: **10.1016/j.actamat.2013.08.031**.

120 P. P. Dholabhai, R. Perriot and B. P. Uberuaga, Atomic-Scale Structure and Stability of the Low-Index Surfaces of Pyrochlore Oxides, *J. Phys. Chem. C*, 2016, **120**(19), 10485–10499, DOI: **10.1021/acs.jpcc.6b02847**.

121 A. Demkov and A. Navrotsky, *Material Fundamentals for Gate Dielectrics*; 2005.

122 C. K. Chung, E. C. O'Quinn, J. C. Neuefeind, A. F. Fuentes, H. Xu, M. Lang and A. Navrotsky, Thermodynamic and Structural Evolution of Mechanically Milled and Swift Heavy Ion Irradiated Er2Ti2O7 Pyrochlore, *Acta Mater.*, 2019, **181**, 309–317, DOI: **10.1016/j.actamat.2019.09.022**.

123 C. K. Chung, J. Shamblin, E. C. O'Quinn, A. Shelyug, I. Gussev, M. Lang and A. Navrotsky, Thermodynamic and Structural Evolution of Dy2Ti2O7 Pyrochlore after Swift Heavy Ion Irradiation, *Acta Mater.*, 2018, **145**, 227–234, DOI: **10.1016/j.actamat.2017.12.044**.

124 C. K. Chung, M. Lang, H. Xu and A. Navrotsky, Thermodynamics of Radiation Induced Amorphization and Thermal Annealing of Dy2Sn2O7 Pyrochlore, *Acta Mater.*, 2018, **155**, 386–392, DOI: **10.1016/j.actamat.2018.06.003**.